

Possibility of cold nuclear compression in antiproton-nucleus collisions

A. B. Larionov,^{1,2,3,*} I. N. Mishustin,^{1,2} L. M. Satarov,^{1,2} and W. Greiner¹

¹Frankfurt Institute for Advanced Studies, J.W. Goethe-Universität, D-60438 Frankfurt am Main, Germany

²Russian Research Center “Kurchatov Institute,” 123182 Moscow, Russia

³Institut für Theoretische Physik, Universität Giessen, D-35392 Giessen, Germany

(Received 16 December 2009; revised manuscript received 23 April 2010; published 3 August 2010)

We study the dynamical response of the ^{16}O nucleus to an incident antiproton using the Giessen Boltzmann-Uehling-Uhlenbeck microscopic transport model with relativistic mean fields. A special emphasis is put on the possibility of a dynamical compression of the nucleus induced by the moving antiproton. Realistic antibaryon coupling constants to the mean meson fields are chosen in accordance with empirical data. Our calculations show that an antiproton embedded in the nuclear interior with momentum less than the nucleon Fermi momentum may create a locally compressed zone in the nucleus with a maximum density of about twice the nuclear saturation density. To evaluate the probability of the nuclear compression in high-energy \bar{p} -nucleus collisions, we adopt a two-stage scheme. This scheme takes into account the antiproton deceleration due to the cascade of $\bar{p}N$ rescatterings inside the nucleus (first stage), as well as the nuclear compression by the slow antiproton before its annihilation (second stage). With our standard model parameters, the fraction of \bar{p} annihilation events in the compressed zone is about 10^{-5} for $\bar{p}^{16}\text{O}$ collisions at $p_{\text{lab}} = 3\text{--}10$ GeV/ c . Finally, possible experimental triggers aimed at selecting such events are discussed.

DOI: [10.1103/PhysRevC.82.024602](https://doi.org/10.1103/PhysRevC.82.024602)

PACS number(s): 25.43.+t, 21.30.Fe, 24.10.Lx

I. INTRODUCTION

The production of compressed nuclear matter in the laboratory is one of the most important achievements of heavy-ion physics during past decades. Heavy-ion-collision experiments open the possibility of studying new phases of matter, such as, for example, a quark-gluon plasma [1,2] (see also Ref. [3] for a recent review). In a heavy-ion collision, compression is accompanied by the strong heating of matter by the shock-wave mechanism [4]. However, very little is known about possible compressional effects induced by a slowly moving or even stopped hadron in a nucleus. In this case, the compression is associated with the enhanced concentration of nucleons around the hadron, provided its interaction with nucleons is sufficiently attractive. Several examples of such systems are under discussion, but their existence is still an open question.

The most famous example of strongly bound hadron-nucleus systems consists of Λ hypernuclei. By measuring the $E2(5/2^+ \rightarrow 1/2^+)$ transition in the $^7_{\Lambda}\text{Li}$ hypernucleus, the shrinkage of the ^6Li core size by $\sim 19\%$ has been found experimentally in Ref. [5]. The hypothetical multistrange nuclei composed of several hyperons (Λ , Ξ^0 , Ξ^-) and nucleons (see Refs. [6,7] and references therein) could be self-bound and have an enhanced baryon density.

As proposed in Ref. [8] on the basis of a phenomenological potential model, hypothetical \bar{K} nuclei could be long-lived and strongly bound compact systems with nucleon density reaching almost $10\rho_0$, where ρ_0 is the normal nuclear-matter density. However, as stated in the recent work by Hayano *et al.* [9], the measurement of $2p$ shift in the $3d\text{--}2p$ transition in kaonic ^4He , eliminating a long-standing discrepancy between

the standard theory and experiment, poses severe limitations on superstrong potentials with such high densities. Moderate compressional (core polarization) effects, up to about $2\rho_0$, have been found within the relativistic mean-field calculations of \bar{K} nuclei done in Ref. [10]. However, the depths of 100–200 MeV for the real part of the \bar{K} -nucleus potential at ρ_0 , which follow from the phenomenological models of Refs. [8,10], are disfavored by the chiral SU(3) models [11–13]. Nevertheless, the existence of strongly bound \bar{K} -nuclear systems largely related to the nature of $\Lambda(1405)$ is still under theoretical debate [14,15] and experimental study [16].

Recently, strong compressional effects have been predicted in the strongly bound \bar{p} -nucleus systems [17,18] in the case of a deep real part of an antiproton optical potential, $\text{Re}(V_{\text{opt}}) \leq (150\text{--}200)$ MeV at ρ_0 . We remark, however, that the antibaryon optical potentials in the nuclear interior are largely unknown and their study requires more efforts [19–25].

In the present work, we extend our previous study of the dynamical compression induced by a stopped antiproton [26] to the case of a *moving* \bar{p} . The calculations are based on the Giessen Boltzmann-Uehling-Uhlenbeck (GiBUU) transport model [27]. First, we study kinematical and geometrical conditions at which an antiproton can generate the increase of nucleon density. Second, by performing the transport simulations of \bar{p} -nucleus collisions we evaluate the actual probability of \bar{p} annihilation in the compressed zone for the beam momenta of 0.3–10 GeV/ c , relevant for future antiproton beams at the Facility for Antiproton and Ion Research (FAIR) in Darmstadt. Finally, we study possible triggering schemes that can be used to select the events with \bar{p} annihilation in the compressed nuclear environment. We have chosen the ^{16}O nucleus as a target. This is motivated by our earlier observation [17,18,26] that the compressional effects associated with \bar{p} are more pronounced in light nuclei.

*Corresponding author: larionov@fias.uni-frankfurt.de

The article is organized as follows: In Sec. II, the description of a calculational procedure is given. Then, in Sec. III, we study the dynamical patterns of the nuclear compression by an antiproton initialized at different momenta and positions inside a nucleus. Sec. IV contains our results on the probabilities of a \bar{p} annihilation in the compressed zone for energetic \bar{p} -nucleus collisions. In Sec. IV, we also discuss possible triggers based on the fast proton emission and on the measurement of the energy deposition. We analyze the influence of the possible in-medium modifications of the \bar{p} -annihilation rate and of the different antiproton mean-field parameters on our results in Sec. V. Summary and outlook are given in Sec. VI.

II. THE CALCULATIONAL PROCEDURE

In our calculations, we apply the GiBUU model [27]. This model solves the coupled set of semiclassical kinetic equations for various hadronic species: nucleons, antinucleons, mesons, baryonic resonances, and their corresponding antiparticles. We use the relativistic mean-field mode of calculations [22,26,28,29], which provides a simple and natural description of both baryonic and antibaryonic mean fields by using the same Lagrangian. The kinetic equation for the hadron of the type j ($j = p, n, \Delta^{++}, \Delta^+, \Delta^0, \Delta^-, \dots, \pi^+, \pi^0, \pi^-, \dots$, and respective antibaryons) reads as

$$\frac{1}{p_0^*} \left[p^{*\mu} \frac{\partial}{\partial x^\mu} + \left(p_\mu^* F_j^{k\mu} + m_j^* \frac{\partial m_j^*}{\partial x_k} \right) \frac{\partial}{\partial p^{*k}} \right] f_j(x, \mathbf{p}^*) = I_j[\{f\}], \quad (1)$$

where $f_j(x, \mathbf{p}^*)$ is the phase-space density of the j th-type particles, p^* is the kinetic four momentum [$p_0^* = \sqrt{\mathbf{p}^{*2} + (m_j^*)^2}$], m_j^* is the effective mass, and $F_j^{k\mu}$ is the field tensor. The left-hand side of Eq. (1) describes the evolution of the phase-space density $f_j(x, \mathbf{p}^*)$ under the influence of the mean mesonic fields. The right-hand side of Eq. (1) is the collision integral $I_j[\{f\}]$ describing the change of the phase-space density due to the particle-particle collisions and resonance decays.

The kinetic equations (1) are solved by applying the standard test particle technique in the parallel ensemble mode. The phase-space densities are represented by the set of the pointlike test particles:

$$f_j(x, \mathbf{p}^*) = \frac{(2\pi)^3}{g_j N_{\text{ens}}} \sum_{i=1}^{N_{\text{ens}} N_j} \delta[\mathbf{r} - \mathbf{r}_i(t)] \delta[\mathbf{p}^* - \mathbf{p}_i^*(t)], \quad (2)$$

where N_j is the number of physical particles of the type j , N_{ens} is the number of parallel ensembles, and g_j is the spin degeneracy. The test-particle representation (2) provides a simple solution of the kinetic equations (1) in terms of the Hamiltonian-like equations for the centroids $[\mathbf{r}_i(t), \mathbf{p}_i^*(t)]$ (cf. Eqs. (2) and (3) in Ref. [22]). The collision integral is simulated with the help of a usual geometrical collision criterion (cf. Ref. [28]).

The mean mesonic fields are determined from the nonlinear Klein-Gordon-like equations, with the source terms given by the particle densities and currents. Therefore, to provide a smooth coordinate dependence of the mean mesonic fields, the

coordinate space δ functions in the right-hand side of Eq. (2) are replaced with the Gaussians of the width $L \simeq 0.5$ –1 fm in actual calculations. Then, for example, the coordinate space density and the scalar density of the j th-type hadrons are computed as

$$\begin{aligned} \rho_j(x) &= \frac{g_j}{(2\pi)^3} \int d^3 p^* f_j(x, \mathbf{p}^*) \\ &= \frac{1}{(2\pi)^{3/2} L^3 N_{\text{ens}}} \sum_{i=1}^{N_{\text{ens}} N_j} \exp \left\{ -\frac{[\mathbf{r} - \mathbf{r}_i(t)]^2}{2L^2} \right\}, \quad (3) \\ \rho_{Sj}(x) &= \frac{g_j}{(2\pi)^3} \int d^3 p^* \frac{m_j^*}{p^{*0}} f_j(x, \mathbf{p}^*) \\ &= \frac{1}{(2\pi)^{3/2} L^3 N_{\text{ens}}} \sum_{i=1}^{N_{\text{ens}} N_j} \frac{m_i^*}{p_i^{*0}} \exp \left\{ -\frac{[\mathbf{r} - \mathbf{r}_i(t)]^2}{2L^2} \right\}. \quad (4) \end{aligned}$$

We are interested, in particular, in the values of the nucleon density $\rho = \rho_p + \rho_n$. The antiproton density $\rho_{\bar{p}}$ and the nucleon scalar density $\rho_S = \rho_{Sp} + \rho_{Sn}$ are also used in the present analysis.

The width L in Eqs. (3) and (4) is a pure numerical parameter of the GiBUU model. Its value is correlated with the number of parallel ensembles and is set equal to the coordinate grid step size (cf. Refs. [26,28]). The physical results do not depend on L , provided that it is small enough to resolve the physical nonuniformities of the system. In the present calculations we use the value $L = 0.5$ fm from our earlier work [26], where we have also studied the influence of L on the compression dynamics.

For the nucleon mean field we apply the nonlinear Walecka model. The nucleon-meson coupling constants and the parameters of the σ -field self-interactions are taken from the NL3 parametrization [30]. This parametrization provides the nuclear matter incompressibility $K = 272$ MeV and the nucleon effective mass $m_N^* = 0.6m_N$ at $\rho_0 = 0.148$ fm $^{-3}$. Within the NL3 set of parameters, the binding energies, charge, and neutron radii of spherical nuclei, as well as deformation properties of some rare-earth and actinide nuclei, have been described quite well [30]. The isoscalar monopole resonance energies in heavy spherical nuclei are also reproduced by this set of parameters [30].

The antinucleon-meson coupling constants are more uncertain. As it is well known, the G -parity transformation of Walecka-type Lagrangians results in too deep antiproton optical potentials. Therefore, following Refs. [18,19,22,26], we introduce a common reduction factor $\xi < 1$ for the antinucleon coupling constants to the σ , ω , and ρ mesons as given by the G -parity transformation. In what follows, if it is not explicitly stated otherwise, we use the value $\xi = 0.22$ obtained in Ref. [22] from the best fit of \bar{p} -absorption cross sections on nuclei at the beam momenta below 1 GeV/ c . The corresponding real part of an antiproton optical potential is about -150 MeV in the nuclear center, which is somewhat deeper than the real part derived from the most recent \bar{p} -atomic

calculations [19], however within the commonly accepted uncertainty interval.¹

Due to a big annihilation cross section, in a majority of events, an antiproton colliding with a nucleus will annihilate already on peripheral nucleons. However, as argued in Ref. [18], compressional effects are expected only in events when the antiproton penetrates deep to the nuclear interior and stops there due to (in)elastic collisions with nucleons. Such events are presumably quite rare and their study requires going beyond the ensemble-averaged description provided by the kinetic mean-field theory. The quantum molecular dynamics [31] or antisymmetrized molecular dynamics [32] models seem to be better theoretical tools for studying such rare events. However, to our knowledge, at present there exists no version of a molecular dynamics model that incorporates all relevant antibaryon-baryon collision channels and relativistic potentials.

In the present work, we treat compressional effects in a \bar{p} -nucleus collision perturbatively. It means that the influence of the compressional response of a nucleus on the deceleration process and eventual annihilation of an antiproton is neglected. Thus, the collisional dynamics of the incident antiproton is simulated within standard GiBUU until its annihilation. We assume further that the position and momentum of the \bar{p} at the beginning of compression process are not much different from those at its annihilation point. Then we study the compressional response of the nucleus to slow antiprotons and evaluate their survival probability.

Therefore, we adopt a two-stage calculational scheme: On the first stage, an antiproton penetrates into the nucleus while experiencing one or more rescatterings on nucleons. We describe this process by the standard GiBUU simulation in the parallel ensemble mode with $N_{\text{ens}} = 1000$ parallel ensembles. Each parallel ensemble is considered as one event. For each impact parameter, $N_{\text{runs}} = 100$ simulation runs have been done, which gives $N_{\text{ens}}N_{\text{runs}} = 10^5$ events per impact parameter. We have chosen 32 impact parameters $b = 0.25, 0.50, \dots, 8$ fm for the $\bar{p}^{16}\text{O}$ system. Final results are impact-parameter weighted. Because the incoming \bar{p} can be transformed to another antibaryons, for example, \bar{n} or $\bar{\Delta}$, we consider in what follows the antibaryon annihilation in general. The coordinates $\mathbf{r}_{\bar{B}}$ and the kinetic three momenta $\mathbf{p}_{\bar{B}}^*$ of an antibaryon just before the annihilation or, for events without annihilation, at the end of the computational time (40 fm/c) have been determined and stored for every event. In the following, we always deal with the kinetic three momenta of particles but omit the word “kinetic” and the star symbol for brevity.² Due to the averaging of the mean field over parallel ensembles, the compressional effects are practically unnoticeable in the standard GiBUU calculation, because rare events with a deep penetration of \bar{p} into the nucleus are diluted with the majority of events when the antiproton annihilates on

the nuclear periphery. This is why we use the coordinates and momenta of the antibaryon obtained on the first stage as an input for another simulation based on the GiBUU model [26,33]. Thus, on the second stage, an antiproton is initialized inside the nucleus at the phase-space point $(\mathbf{r}_{\bar{B}}, \mathbf{p}_{\bar{B}})$ using the Gaussian distribution in coordinate space and the sharp-peaked distribution in momentum space. By doing so we neglect the possibility that the annihilating antibaryon can be different from the antiproton. This is, however, not important in view that the mean-field contributions, apart from small isospin and Coulomb effects, are the same for all antibaryons in our model. The corresponding phase-space density of an antiproton is written as ($\hbar = c = 1$)

$$f_{\bar{p}}(\mathbf{r}, \mathbf{p}) = \frac{1}{(2\pi)^{3/2}\sigma_r^3} \exp\left\{-\frac{(\mathbf{r} - \mathbf{r}_{\bar{B}})^2}{2\sigma_r^2}\right\} \frac{(2\pi)^3}{g_{\bar{p}}} \delta(\mathbf{p} - \mathbf{p}_{\bar{B}}), \quad (5)$$

where $g_{\bar{p}} = 2$ is the spin degeneracy of an antiproton and σ_r is the width of the coordinate space Gaussian. Please notice that the quantity σ_r is a physical parameter of our model, while the quantity L in Eqs. (3) and (4) is pure technical and should not be misidentified with σ_r . We stress that now the antiproton test particles of all N_{ens} parallel ensembles are initialized according to Eq. (5) with the same centroid $(\mathbf{r}_{\bar{B}}, \mathbf{p}_{\bar{B}})$, and the calculation is repeated for every event of the first stage. Thus, the antiproton test particle contributions to the mean mesonic fields reflect the presence of a real antiproton at the phase-space point $(\mathbf{r}_{\bar{B}}, \mathbf{p}_{\bar{B}})$. In this new calculation, therefore, the compressional effects will manifest themselves in full strength without dilution. Further evolution of the \bar{p} -nucleus system is calculated in a similar way as in Ref. [26] by using the GiBUU model without annihilation. However, in distinction to Ref. [26], we now take into account all collisional channels different from the annihilation one, in particular, $NN \rightarrow NN$ and $\bar{N}N \rightarrow \bar{N}N$. This models dissipation leading to some small heating of the nuclear system and slowing down the antiproton during compression process. For brevity, sometimes we refer to the GiBUU calculations without annihilation as “coherent” calculations in what follows.

Instead of explicitly treating the annihilation on the second stage of calculations, we compute the survival probability of an antiproton in the course of compression as

$$P_{\text{surv}}(t) = \exp\left\{-\int_0^t dt' \Gamma_{\text{ann}}(t')\right\}. \quad (6)$$

Here

$$\Gamma_{\text{ann}} = \langle v_{\text{rel}} \sigma_{\text{ann}} \rangle \rho \quad (7)$$

is the antiproton width with respect to the annihilation, ρ is the local nucleon density, v_{rel} is the relative velocity of an antiproton and a nucleon, and σ_{ann} is the \bar{p} -annihilation cross section on a nucleon. Brackets in Eq. (7) denote averaging over the nucleon Fermi motion.

The two-stage scheme described earlier is not fully equivalent to the true molecular-dynamics simulation. However, the most interesting phenomenon that we want to study, that is, the dynamical compression of a nucleus by a slow antiproton, can be realistically simulated in this way.

¹For detailed discussion, see Ref. [22] and references therein.

²In fact, if the collective motion of nuclear matter is negligible, for example, when a fast hadron passes through the undisturbed nuclear target, the space components of the canonical and kinetic four momenta are practically the same.

As we see in what follows (cf. Figs. 1 and 7), the width σ_r of the Gaussian in Eq. (5) is a very important parameter, which cannot be determined from our model. We therefore consider two most representative values: $\sigma_r = 1$ fm and $\sigma_r = 0.14$ fm. The first choice corresponds to a rather wide wave packet which presumably describes the static wave function of a strongly bound antiproton implanted in a nucleus [17,18,26]. The second choice of a narrow wave packet is adjusted to describe the charge rms radius of a physical (anti)proton, $r_p = 0.9$ fm [34]. Indeed, in our model, the true source charge distribution of an antiproton is given by folding the coordinate space Gaussian (5) with the test particle Gaussian. Thus, we have $\sigma_p = \sqrt{\sigma_r^2 + L^2}$, where $\sigma_p = r_p/\sqrt{3}$ is the charge distribution width of a physical (anti)proton.

The second-stage calculations can be significantly accelerated if one neglects the changes in a target nucleus caused by the antiproton cascade on the first stage. Then the spherical symmetry of the ^{16}O target nucleus can be utilized. In this case, the compressional evolution depends only on three variables: the absolute values of the antiproton initial radius-vector \mathbf{r} and momentum \mathbf{p} and the angle $\Theta = \arccos(\mathbf{r}\mathbf{p}/rp)$ between \mathbf{r} and \mathbf{p} . (One needs six variables \mathbf{r} , \mathbf{p} in the case of arbitrary shape.) Therefore, the second-stage calculations have been performed with the target nucleus for the set of the antiproton initial positions \mathbf{r} and momenta \mathbf{p} taken on the uniform $7 \times 20 \times 9$ grid in the space $(r, p, \cos \Theta)$, where $r \in [0.5; 3.5]$ fm, $p \in [0.05; 1.00]$ GeV/c, and $\cos \Theta \in [-1; 1]$. The results of the second-stage calculations, in particular, the antiproton survival probabilities at the time moments corresponding to the system entering to and exiting from the compressed state, have been stored. To determine the compression probability for a given first-stage event, resulting coordinates and momenta of the antibaryon at the annihilation point have been projected on the grid.

III. DYNAMICS OF NUCLEAR COMPRESSION

In this section, the nuclear response to the moving antiproton is considered disregarding \bar{p} annihilation. The latter is, however, implicitly taken into account by following the time dependence of the \bar{p} -survival probability.

Figure 1 shows the time evolution of the nucleon and antiproton density distributions for the $\bar{p}^{16}\text{O}$ system for different \bar{p} initializations. Only the cases where the initial antiproton momentum \mathbf{p} is (anti)parallel to the initial position vector \mathbf{r} , that is, $\Theta = 0$ and $\Theta = \pi$, are presented.

Let us start by considering how compression depends on the initial antiproton coordinate z at fixed momentum $p = 0.3$ GeV/c. If the antiproton moves toward the nuclear center, that is, $\Theta = \pi$, the compression of a nuclear system up to densities $\sim 2\rho_0$ is reached within the time interval of about 10 fm/c [see panels (a)–(d) and (e)–(h) of Fig. 1]. For the outgoing antiproton ($\Theta = 0$), the compression is much smaller [panels (i)–(l) of Fig. 1] because the antiproton moves through the nuclear periphery. It is interesting that at $p = 0.3$ GeV/c the antiproton does not leave the nucleus but only bounces off the nuclear boundary and finally gets captured. However, the capture takes place on the time scale of ~ 20 fm/c and

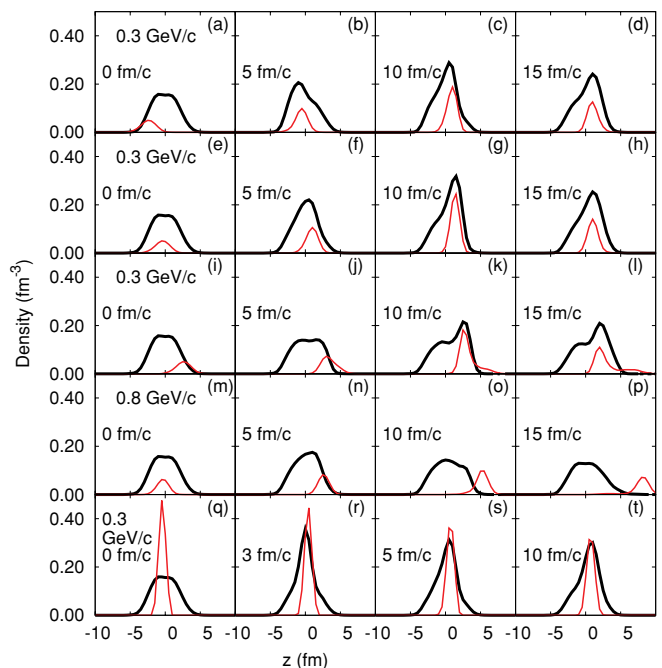


FIG. 1. (Color online) Nucleon (thick black lines) and antiproton (thin red lines) densities as functions of the longitudinal coordinate z at different time moments for the $\bar{p}^{16}\text{O}$ system. The antiproton has been initialized on the axis passing through the nuclear center; that is, $x = y = 0$ with momentum p along the positive z direction. Different rows correspond to different \bar{p} initializations characterized by the Gaussian width σ_r (fm), momentum p (GeV/c), and coordinate z (fm): (a)–(d) $(\sigma_r, p, z) = (1, 0.3, -2.5)$; (e)–(h) $(1, 0.3, -0.5)$; (i)–(l) $(1, 0.3, 2.5)$; (m)–(p) $(1, 0.8, -0.5)$; (q)–(t) $(0.14, 0.3, -0.5)$. The antibaryon annihilation is switched off in this calculation.

therefore would hardly be observed due to a very low survival probability of the antiproton (see Fig. 2).

For a higher momentum $p = 0.8$ GeV/c [panels (m)–(p) of Fig. 1], the compression is practically absent because the nuclear response is much slower than the time needed by the antiproton to cross the nucleus. We also see that at $p = 0.8$ GeV/c the antiproton escapes from the nucleus because its total in-medium energy $E_{\bar{p}} = \sqrt{\mathbf{p}^2 + m_{\bar{p}}^{*2}} + V_{\bar{p}}^0$ exceeds the vacuum mass m_N by about 165 MeV. Here $m_{\bar{p}}^* = m_N + \xi(m_N^* - m_N) \simeq 0.91m_N$ is the antiproton effective mass and $V_{\bar{p}}^0 = -(308\xi)\text{MeV} \simeq -68$ MeV is the antiproton vector potential at $\rho = \rho_0$.

The compression process is quite sensitive to the choice of initial Gaussian width of the antiproton. One can see this from Fig. 1 by comparing panels (e)–(h) and (q)–(t), where the calculations are shown for the same initial positions and momenta of \bar{p} , but for the different widths σ_r . Due to a deeper nucleon potential, a smaller initial \bar{p} width makes the compression more pronounced and fast. Unless stated otherwise, the case of $\sigma_r = 1$ fm is discussed in what follows.

In Fig. 2, we present the time dependence of the maximum nucleon density ρ_{max} and of the antiproton survival probability (6) for various antiproton initializations shown in Fig. 1. As we have already seen in Fig. 1, for the initializations

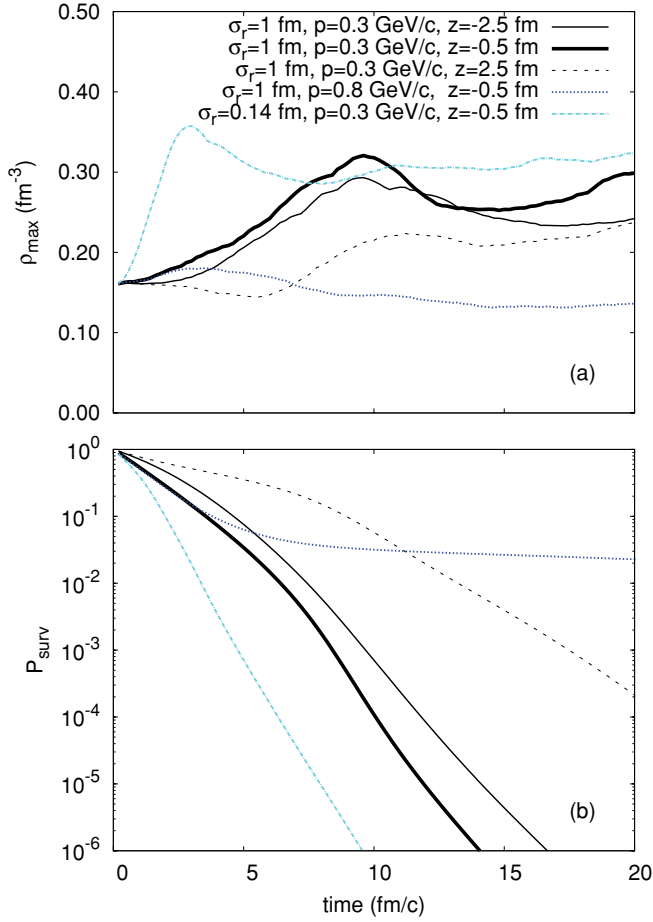


FIG. 2. (Color online) Maximum nucleon density (a) and antiproton survival probability (b) as functions of time for the $\bar{p}^{16}\text{O}$ system. Different curves correspond to different \bar{p} initializations, as explained in Fig. 1.

with $z < 0$ (i.e., for $\Theta = \pi$) and $p = 0.3$ GeV/c, nucleon densities up to $2\rho_0$ are reached. The antiproton survives with the probability $P_{\text{surv}} \sim 10^{-2}$ until the time moment when the maximum density $\rho_{\max} = 2\rho_0$ is achieved.

The nuclear compression caused by an antiproton could only be observed, if the antiproton would annihilate in the compressed nuclear environment. This process can be detected by its specific final-state characteristics. As shown in Refs. [18,26], possible observable signals include the enhanced radial collective flow of nuclear fragments, hardening the energy spectra of emitted nucleons, and softening the meson-invariant mass distributions. Moreover, the multinucleon annihilation (MNA) channels with the baryonic number $B \geq 1$ might be enhanced if the compressed zone is formed. A more exotic scenario, the deconfinement of an annihilation zone leading to the enhanced strangeness production, has also been discussed in literature [18,35–37]. Herein we do not consider any specific signals caused by annihilation in the compressed nuclear state. We rather concentrate on the evaluation of the total \bar{p} -annihilation probability at enhanced nucleon densities. For brevity, we refer to this possibility as to the annihilation in a compressed zone (ACZ) in what follows.

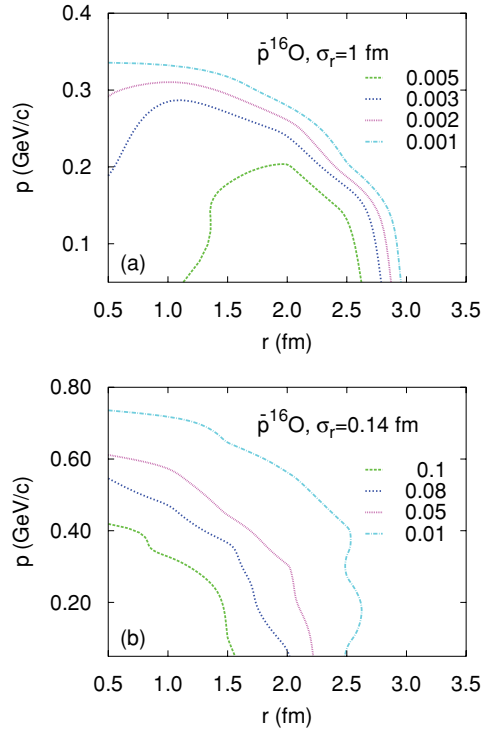


FIG. 3. (Color online) The contour plots of the antiproton ACZ probability P_{ann}^c at $\rho_{\max} > 2\rho_0$ [see Eq. (8)] in the plane given by initial values of the antiproton radial position r and momentum p for the system $\bar{p}^{16}\text{O}$. The values of P_{ann}^c are averaged over the cosine of the angle between the initial radius vector and momentum of the antiproton. Panel (a)[(b)] corresponds to the initial antiproton width $\sigma_r = 1(0.14)$ fm.

Let us define the compressed nuclear system as a system where the maximum nucleon density ρ_{\max} exceeds some critical value ρ_c . If not stated otherwise, we choose $\rho_c = 2\rho_0$ in calculations. Such density values can be reached, for example, in central heavy-ion collisions at beam energies of hundreds of MeV/nucleon [38]. The probability for the antiproton to annihilate at $\rho_{\max} > \rho_c$ is defined as

$$P_{\text{ann}}^c = P_{\text{surv}}(t_1) - P_{\text{surv}}(t_2), \quad (8)$$

where the time interval $[t_1; t_2]$ encloses the high-density phase of the time evolution; that is, $\rho_{\max}(t_1) = \rho_{\max}(t_2) = \rho_c$ with $\rho_{\max}(t) > \rho_c$ for $t_1 < t < t_2$.³ For example, in the case $(\sigma_r, p, z) = (1 \text{ fm}, 0.3 \text{ GeV}/c, -0.5 \text{ fm})$ we obtain $t_1 = 8.4 \text{ fm}/c$ and $t_2 = 11 \text{ fm}/c$ (see Fig. 2). Because the \bar{p} survival probability drops exponentially with time, we have $P_{\text{surv}}(t_1) \gg P_{\text{surv}}(t_2)$ and, therefore, actually $P_{\text{ann}}^c \simeq P_{\text{surv}}(t_1)$.

Figure 3 shows the antiproton ACZ probability as a function of the \bar{p} initial radial position and momentum. As expected, the \bar{p} initializations with smaller momentum lead to larger P_{ann}^c . The radial dependence of P_{ann}^c at fixed initial momentum is somewhat more complicated. In the case of a larger width of the initial antiproton space distribution ($\sigma_r = 1$ fm), P_{ann}^c

³When there are more than one such interval, the earliest one is chosen.

has a weak maximum at $r \simeq 1\text{--}2$ fm and decreases toward the nuclear center slightly. This can be traced back to Fig. 1, where we see that the \bar{p} initializations at different positions result in practically the same compressional effect provided that the antiproton moves to the nuclear center [cf. panels (a)–(d) and (e)–(h)]. For a narrower initial antiproton space distribution ($\sigma_r = 0.14$ fm), the maximum of the ACZ probability is located at the nuclear center, because compression is much faster in this case, and, thus, is more sensitive to the local nucleon density.

IV. \bar{p} -NUCLEUS COLLISIONS

As it was demonstrated in the previous section (cf. Fig. 3), the ACZ probability depends on the position and momentum of the antiproton at the beginning of compression process. Therefore, before discussing the results of a full two-stage calculation, it is instructive to study the distributions of antibaryon annihilation points in the coordinate and momentum space. These distributions are determined at the first stage of calculations.

Figure 4 shows the radial distributions of the antibaryon annihilation points for the $\bar{p}^{16}\text{O}$ reaction at several beam momenta. For inclusive events (a), the maxima of these distributions are located at the peripheral region, where the density is about 30% of the central density, independent of the beam momentum. This is a pure geometrical effect caused by mixing of events with all possible impact parameters. However, for central collisions (b), the maxima are shifted closer to the nuclear center. The shift becomes larger at higher beam momenta. This is expected, because with increasing p_{lab} the \bar{p} -nucleon annihilation cross section drops [39], leading to the larger fraction of deeply located annihilations.

Figure 5 demonstrates the momentum distributions of antibaryons at the annihilation points. There is only a little difference between the shapes of the distributions for the inclusive (a) and central (b) events at the same beam momentum. However, the total annihilation probability is increased by a factor of 3–10 for the central collisions, which is also seen in Fig. 4. The distributions have a sharp peak at the beam momentum and a long tail toward small momenta. In the case of the smallest beam momentum $p_{\text{lab}} = 0.3$ GeV/c, the peak is broader and shifted to the higher momenta $p > p_{\text{lab}}$ for the central collisions. This is caused by the antiproton elastic collisions with the Fermi sea nucleons and by the antibaryon acceleration in a strongly attractive mean-field potential.

The acceleration is better visible in Fig. 6, which shows the correlation between the radial position and the momentum of an antibaryon at the annihilation point. The centrality dependence is quite weak in this case; thus, we have presented the results for the inclusive event set only. For $p_{\text{lab}} = 0.3$ GeV/c, the average momentum of annihilating antibaryon increases up to 0.5 GeV/c at the nuclear center. For larger beam momenta, the mean field acceleration is hindered by the collisional damping of an initial \bar{p} momentum.

We now discuss the results of the full two-stage calculations (see Sec. II). The total annihilation cross section on a nucleus σ_{ann} and the ACZ cross section σ_{compr} are determined as

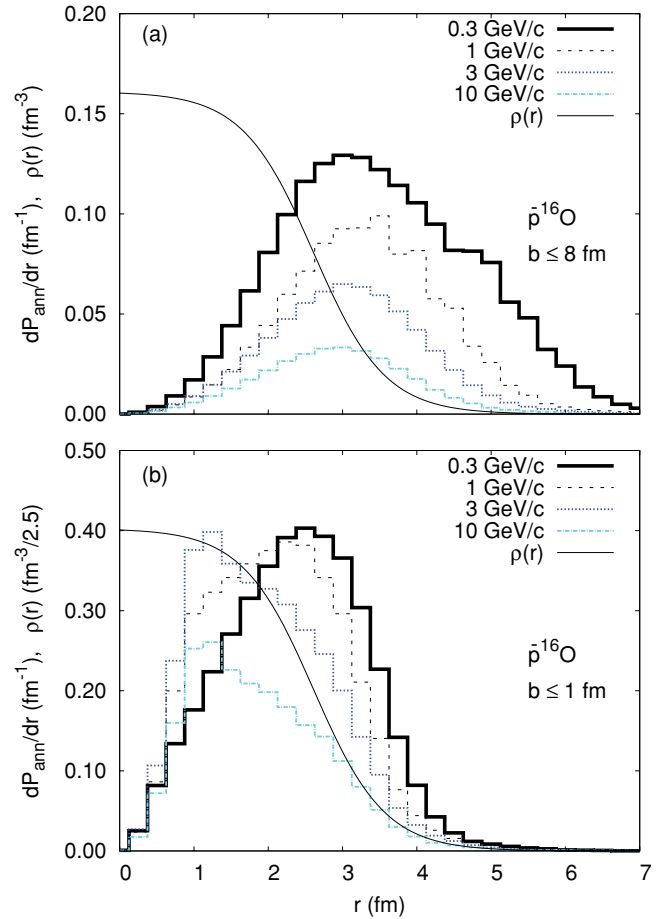


FIG. 4. (Color online) Radial distributions of annihilation points for $\bar{p}^{16}\text{O}$ collisions at different beam momenta (see key notations) normalized to the total annihilation probability. For reference, thin solid lines show the nucleon density profile of the ^{16}O nucleus. Panels (a) and (b) represent the inclusive spectra ($b \leq 8$ fm) and the spectra for central collisions ($b \leq 1$ fm), respectively. Note different scales of vertical axes in panels (a) and (b).

follows:

$$\sigma_{\text{ann}} = \sum_{b \leq b_{\text{max}}} 2\pi b \Delta b \frac{N_{\text{ann}}(b)}{N_{\text{ev}}(b)}, \quad (9)$$

$$\sigma_{\text{compr}} = \sum_{b \leq b_{\text{max}}} 2\pi b \Delta b \frac{1}{N_{\text{ev}}(b)} \sum_{i=1}^{N_{\text{ann}}(b)} P_{\text{ann}}^c(\mathbf{r}_i, \mathbf{p}_i). \quad (10)$$

Here $N_{\text{ev}}(b)$ and $N_{\text{ann}}(b)$ are, respectively, the total number of events and the number of annihilation events calculated within standard GiBUU (the first stage) for a given impact parameter b . The quantity $P_{\text{ann}}^c(\mathbf{r}_i, \mathbf{p}_i)$ [see Eq. (8)], which depends on the annihilation point position \mathbf{r}_i and momentum \mathbf{p}_i in a given annihilation event i , is the annihilation probability at $\rho_{\text{max}} > \rho_c$ computed within a coherent GiBUU run (the second stage). The cutoff value of the impact parameter b_{max} has been chosen to be 8 fm for an inclusive event set and 1 fm for central events.

Figure 7 shows the annihilation cross section σ_{ann} (a) and the relative fraction of ACZ $\sigma_{\text{compr}}/\sigma_{\text{ann}}$ (b) as functions of the beam momentum. While σ_{ann} drops with increasing p_{lab} due to the momentum dependence of the $\bar{p}N$ annihilation

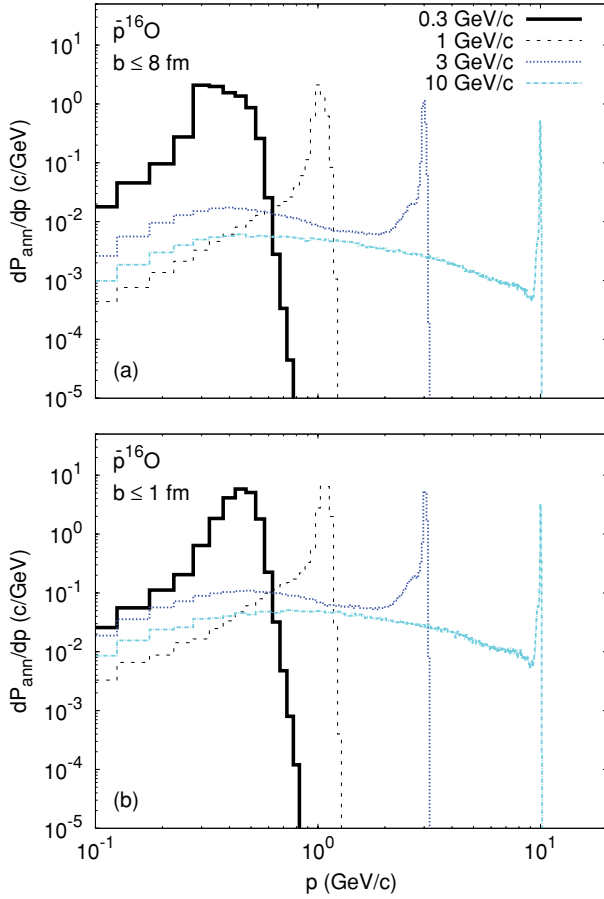


FIG. 5. (Color online) Momentum distributions of annihilation points for $\bar{p}^{16}\text{O}$ collisions at different beam momenta (see key notations). Panels (a) and (b) represent the inclusive spectra and the spectra for the central collisions, respectively.

cross section, the ratio $\sigma_{\text{compr}}/\sigma_{\text{ann}}$ reveals an interesting nonmonotonic behavior. First, it drops with increasing beam momentum up to $p_{\text{lab}} \simeq 1 \text{ GeV}/c$ and then starts to increase

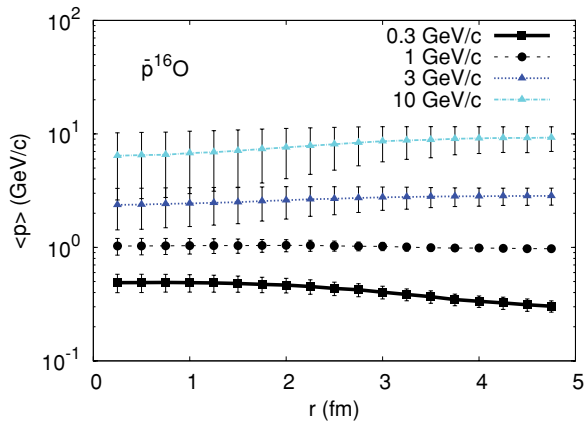


FIG. 6. (Color online) Average momentum of annihilating antibaryon as a function of the radial position for the inclusive set of events $\bar{p}^{16}\text{O}$ at different beam momenta. The error bars represent the dispersion of momentum distribution at a given r .

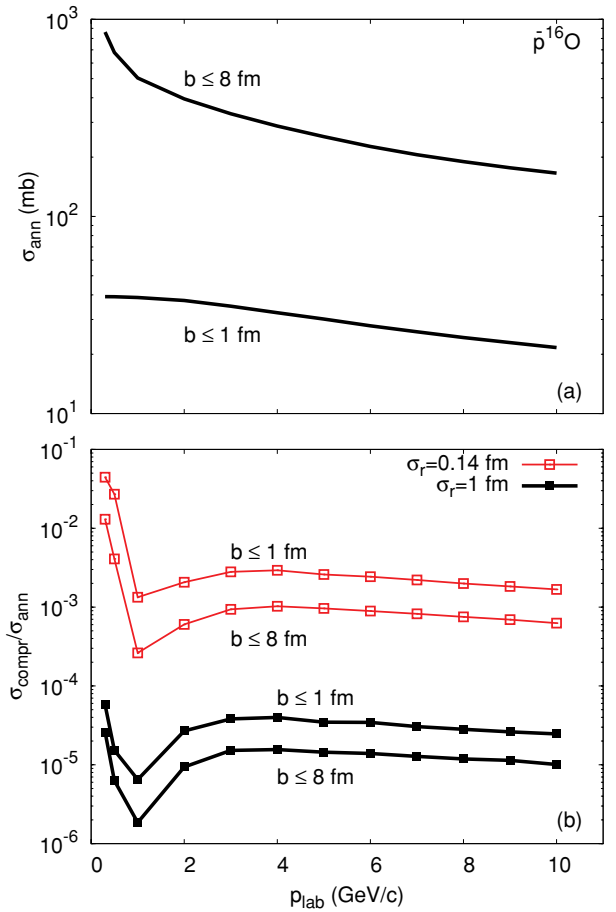


FIG. 7. (Color online) Antiproton annihilation cross section on ^{16}O (a) and the probability of annihilation at $\rho_{\text{max}} > 2\rho_0$ (b) vs a beam momentum. Different lines correspond to different centralities: $b \leq 8 \text{ fm}$, inclusive set of events; $b \leq 1 \text{ fm}$, central events. The cases of a narrow ($\sigma_r = 0.14 \text{ fm}$) and a wide ($\sigma_r = 1 \text{ fm}$) initial antiproton space distribution are depicted in panel (b) by lines with open and solid squares, respectively.

saturation at $p_{\text{lab}} \simeq 3 \text{ GeV}/c$. The growth of this ratio at $p_{\text{lab}} > 1 \text{ GeV}/c$ is caused by opening the inelastic production channels $\bar{N}N \rightarrow \bar{N}N\pi$ with the threshold beam momentum $p_{\text{thr}} = 0.787 \text{ GeV}/c$, $\bar{N}N \rightarrow \bar{N}N\pi\pi$ with $p_{\text{thr}} = 1.210 \text{ GeV}/c$, etc. The inelastic production leads to the additional deceleration of an antibaryon and, therefore, increases the probability of the nuclear compression [18] (see also Fig. 8). Selecting the central events increases the ratio $\sigma_{\text{compr}}/\sigma_{\text{ann}}$ by about a factor of three, which is caused by a larger relative fraction of annihilations at small radii [cf. Fig. 4(b)].

The important result of the previous section is that only a slow antiproton can induce nuclear compression. In practice, we have used the ensemble of annihilation points to initialize the coherent GiBUU runs assuming that antiprotons become slow not far away from their annihilation points. To check this assumption, we have performed additional calculations with other transition criteria from collisional deceleration stage to the coherent compression dynamics. In the first calculation, we have generated the ensemble of points where the momenta \mathbf{p} and coordinates \mathbf{r} of antibaryons satisfy the

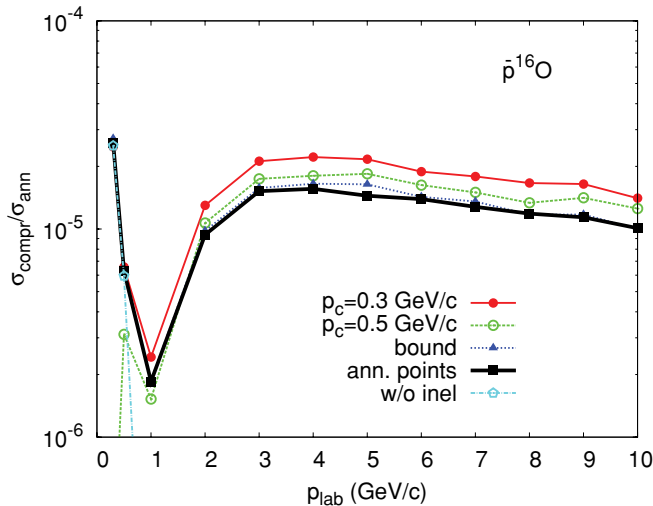


FIG. 8. (Color online) Same as in Fig. 7(b) for the inclusive event set with $\sigma_r = 1$ fm, but for different criteria of transition to the coherent compression dynamics (see text). The lines with solid and open circles represent, respectively, the results obtained with a criterion using the critical momentum $p_c = 0.3$ and 0.5 GeV/c, respectively. The line with solid triangles corresponds to the criterion requiring that the antibaryon becomes bound. The line with solid squares shows the calculation with the default criterion using the annihilation points, the same as in Fig. 7(b). Additionally, the line with open pentagons shows the results obtained by switching off the inelastic channels of the $\bar{N}N$ scattering. In this case, the ACZ probability quickly drops with increasing beam momentum and becomes less than 10^{-8} at $p_{\text{lab}} > 1$ GeV/c.

conditions $|\mathbf{p}| < p_c$ and $|\mathbf{r}| < r_c$ simultaneously, that is, when the antibaryons become slow enough and close enough to the nuclear center. Here, p_c and r_c are parameters to be chosen. As follows from Fig. 3, the choice $p_c \simeq 0.3\text{--}0.5$ GeV/c, $r_c \simeq 3$ fm provides almost the full coverage of the (r, p) region where a significant ($\rho > 2\rho_0$) compression is expected. Another criterion selects the antibaryon momentum and position at the first time instant, when the antibaryon becomes bound, that is, its energy falls below its bare mass. Figure 8 shows the ACZ probability calculated by using the different transition criteria. All results are quite similar, except for the calculation with $p_c = 0.5$ GeV/c which becomes unphysical at $p_{\text{lab}} < p_c$.

To give more insight into the \bar{p} -induced nuclear compression, in Figs. 9 and 10 we show the distributions of annihilation events on the longitudinal coordinate z and the longitudinal momentum p_z of the antibaryon for central (a) and peripheral (c) $\bar{p}^{16}\text{O}$ collisions. The relative probability of annihilation in the compressed zone as a function of z and p_z is shown in panels (b) and (d) for central and peripheral collisions, respectively. Independent of the beam momentum, the maximum ACZ probability is reached if the antibaryon is stopped in the central region. However, the longitudinal coordinates for events most favorable for compression are rather uncertain, as expected already from Fig. 1. On the other hand, we definitely observe a rather strong impact parameter dependence with the clear preference of central collisions for selecting the ACZ events. At large beam momenta (Fig. 10), the compression

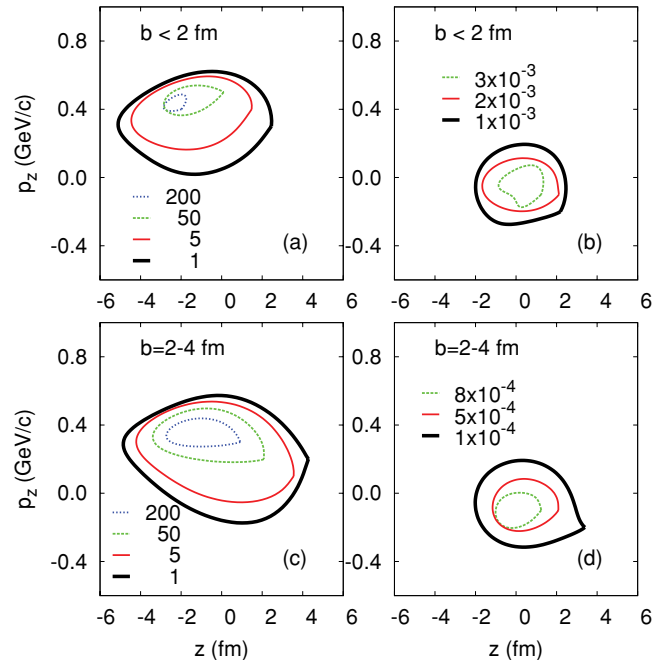


FIG. 9. (Color online) Panels (a) and (c) show the contour lines of the antiproton annihilation cross section $d\sigma_{\text{ann}}/(dzdp_z)$ [mb/(fm GeV/c)] in the plane of longitudinal coordinate z and longitudinal momentum p_z of the annihilation points for central (a) and peripheral (c) collisions. Panels (b) and (d) show the contour lines of relative fraction of annihilations at high density ($\rho_{\text{max}} > 2\rho_0$), $\sigma_{\text{compr}}/\sigma_{\text{ann}}$, in the same plane for central (b) and peripheral (d) collisions. The colliding system is $\bar{p}^{16}\text{O}$ at 0.3 GeV/c.

can only be reached at the extreme tail of the antibaryon longitudinal momentum distribution, and the total probability of ACZ is small. As one can see from the right panels in Figs. 9 and 10, a significant compression ($\rho_{\text{max}} > 2\rho_0$) can be produced by antibaryons whose longitudinal momenta are less than 200 MeV/c. However, the maximum relative probability of ACZ in the (z, p_z) plane is practically independent on the beam momentum. This is expected because in our model the probability of ACZ depends only on the position and momentum of the antibaryon prior the annihilation.

Because nuclear compression is most probable for stopped annihilations, one needs a trigger to select the events with slow antiprotons. We discuss two possible triggers here.

The first trigger requires the detection of a fast proton in the forward direction [21]. The idea behind this is that the incoming antiproton can be decelerated and captured in a nucleus by experiencing a hard collision with a single nucleon.

Figure 11(a) shows the cross section $\sigma_{p_{\text{min}}}$ of an antiproton annihilation on ^{16}O accompanied by the emission of a proton with momentum exceeding some value p_{min} as a function of p_{min} . For simplicity, we did not apply any angular cuts for the proton momentum. At large beam momenta, 3 and 10 GeV/c, the cross section $\sigma_{p_{\text{min}}}$ sharply drops with p_{min} near $p_{\text{min}} \simeq p_{\text{lab}}$. In panel (b) of Fig. 11, we show the relative fraction $\sigma_{\text{compr}}/\sigma_{p_{\text{min}}}$ of ACZ as a function of the minimum proton momentum p_{min} . For $p_{\text{lab}} = 3$ and 10 GeV/c, the quantity

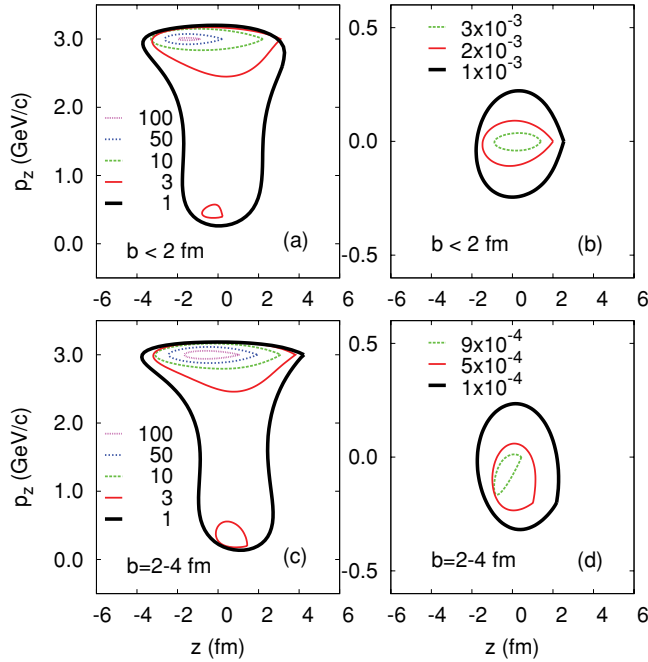


FIG. 10. (Color online) Same as Fig. 9, but for $p_{\text{lab}} = 3 \text{ GeV}/c$. Notice different scales of vertical axes in the left and right panels.

$\sigma_{\text{compr}}/\sigma_{p_{\text{min}}}$ grows by almost a factor of 30 while p_{min} increases from zero to p_{lab} .

Emission of a fast proton with momentum close to the \bar{p} -beam momentum can be caused by the following mechanisms: (i) elastic scattering $\bar{p} + p \rightarrow \bar{p}_{\text{slow}} + p_{\text{fast}}$, (ii) inelastic production processes of the type $\bar{p} + p \rightarrow \bar{p}_{\text{slow}} + p_{\text{fast}} + \text{mesons}$, and (iii) collisions with high-momentum annihilational pions, $\pi + p \rightarrow p_{\text{fast}} + X$. We have checked that inelastic reactions (ii) give the largest contribution to the production of the fast proton at $p_{\text{lab}} = 3$ and $10 \text{ GeV}/c$. This makes the fast proton trigger rather efficient at high beam momenta. The contribution from process (iii) is relatively small, while elastic scattering (i) practically does not contribute to the yield of fast protons at $p_{\text{lab}} = 3$ and $10 \text{ GeV}/c$. However, for small beam momenta, 0.3 and $1 \text{ GeV}/c$, the pionic mechanism (iii) contributes dominantly to the fast proton yield with only a small admixture of elastic scattering (i). Therefore, the trigger based on a fast proton in final state is ineffective at small beam momenta.

The second possible trigger is based on the energy deposition [40,41],

$$E_{\text{dep}} = T_{\bar{p}} + 2m_N - \sum_i E_{\text{mes}}^{(i)}, \quad (11)$$

where $T_{\bar{p}}$ is the antiproton beam energy, $E_{\text{mes}}^{(i)}$ is the energy of i th outgoing meson, and the sum runs over all produced mesons in a given event. Neglecting nucleon and antibaryon binding energy, antiproton elastic and inelastic scattering before annihilation and final-state interactions of produced mesons, one has $E_{\text{dep}} = 0$. In the case of low-energy antiproton-nucleus collisions, annihilations with a larger energy deposition occur deeper in the nucleus, as was found in Ref. [40]. The

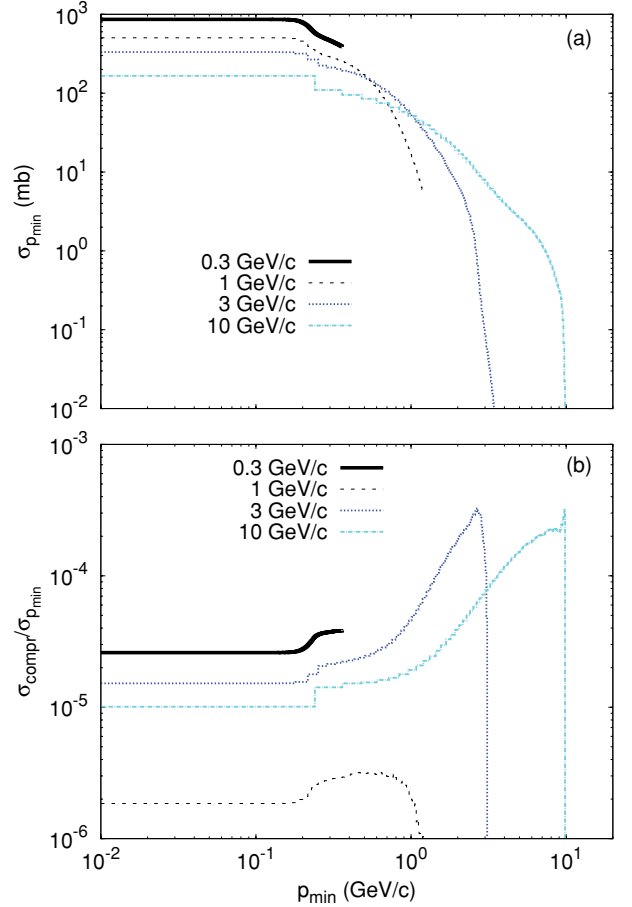


FIG. 11. (Color online) (a) The cross section $\sigma_{p_{\text{min}}}$ of \bar{p} annihilation on ^{16}O accompanied by the emission of a proton with momentum larger than p_{min} as a function of p_{min} . (b) The relative probability $\sigma_{\text{compr}}/\sigma_{p_{\text{min}}}$ of the annihilation in the compressed zone ($\rho_{\text{max}} > 2\rho_0$) vs the minimum momentum p_{min} of the emitted proton. Different curves refer to different \bar{p} -beam momenta.

explanation was that the annihilation mesons lose their energy or get absorbed more effectively if the annihilation takes place deeply inside the nucleus. For high-energy \bar{p} -nucleus interactions, the incoming antiproton can rescatter before annihilation transferring a part of energy to the nucleons. This also leads to larger values of E_{dep} because the produced mesons will have a smaller total energy in this case. Both types of events, deep and/or slow antibaryon annihilations, should be of the ACZ type with an increased probability. Results for E_{dep} trigger are shown in Fig. 12. As one can see, triggering on a large energy deposition, $E_{\text{dep}} \simeq T_{\bar{p}} + 2m_N$, increases the fraction of ACZ events by about a factor of 30 with respect to $E_{\text{dep}} \simeq 0$ for the beam momentum of $10 \text{ GeV}/c$.

V. IN-MEDIUM MODIFICATIONS OF ANTIPROTON ANNIHILATION

So far we have used the vacuum $\bar{p}N$ annihilation cross section and the fixed antibaryon mean-field parameters. As the survival probability of an antiproton (6) is determined by its annihilation width (7), it is important to consider possible

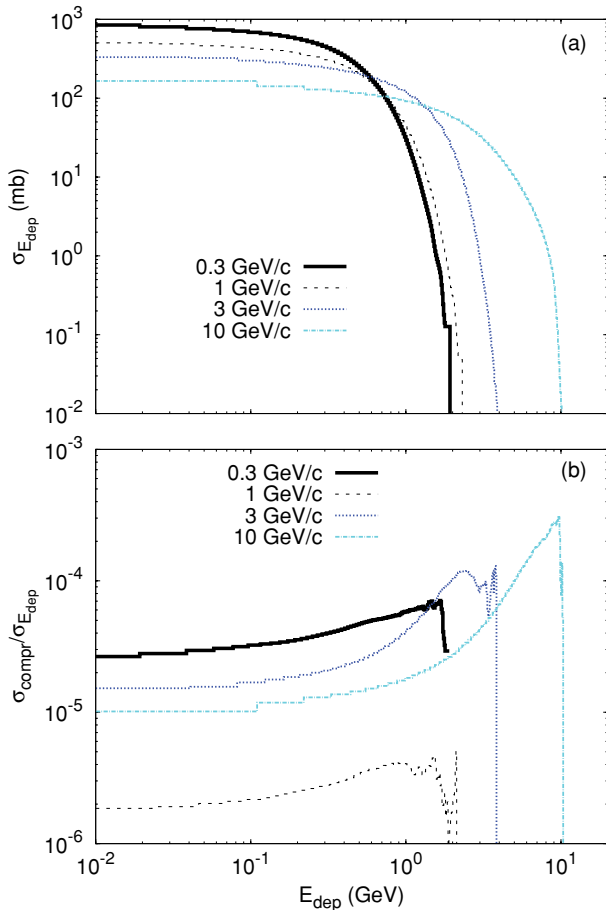


FIG. 12. (Color online) (a) Antiproton annihilation cross section on ^{16}O at the condition of the energy deposition exceeding E_{dep} as a function of E_{dep} . (b) The relative probability $\sigma_{\text{compr}}/\sigma_{E_{\text{dep}}}$ of a compressional annihilation ($\rho_{\text{max}} > 2\rho_0$) as a function of E_{dep} . Different curves correspond to different \bar{p} -beam momenta.

in-medium modifications of the latter. At the same time, the speed and the amplitude of the nuclear compression depend on the value of the reduction factor ξ of the antibaryon-meson coupling constants [26]. Thus, the probability of ACZ is the result of the competition between compression and annihilation. In this section, we discuss possible modifications of the antiproton annihilation width in nuclear medium. The sensitivity of our results to the in-medium modifications is demonstrated in Fig. 15.

As discussed by many authors (see, e.g., Refs. [18, 23–25, 35, 42–46]), the annihilation rate of antiprotons in a dense nuclear medium may significantly differ from simple calculations using the vacuum $\bar{p}N$ annihilation cross section σ_{ann} [see Eq. (7)]. There are several effects that become important at sufficiently high nucleon densities. First, the dispersion relations of nucleons and antinucleons are modified due to interactions with mean mesonic fields. In particular, the effective masses m_N^* and $m_{\bar{N}}^*$ are reduced compared to the vacuum value. Generally, this leads to the reduction of the imaginary parts of the nucleon and antinucleon self-energies in nuclear medium. The influence of the baryon and antibaryon in-medium dispersion relations on the antibaryon

annihilation rate has been studied in Ref. [18]. Other examples of the influence of the baryonic effective masses on hadronic processes are the in-medium reduced cross sections of the NN elastic scattering [47, 48] and of the Δ -resonance production $NN \rightarrow N\Delta$ [49, 50]. As an illustrative example of the in-medium reduction caused by effective masses, we consider the two-pion annihilation channel later in this section.

Another important in-medium effect is the appearance of the MNA channels. The famous Pontecorvo reaction [51] $\bar{p}d \rightarrow \pi^- p$ is an example of the MNA processes. It is commonly believed that MNA is responsible for the emission of high-energy protons from low-energetic \bar{p} annihilation on nuclei [24, 52, 53]. Moreover, the triggering on high-momentum protons is already applied in experimental techniques to distinguish MNA from the single-nucleon annihilation (SNA) followed by the final-state interaction (rescattering and absorption) of produced mesons [53].

Up to now the attempts to estimate the MNA contribution performed by different theoretical and experimental groups did not lead to definite conclusions. The experimental determinations of the MNA probability give values of about 10%–30% for the \bar{p} annihilations at rest [52, 53]. One has to admit that these values agree with predictions of Hernández and Oset (HO) [23–25]. It is important for this agreement, however, that the annihilations of stopped antiprotons take place *at the nuclear fringe*, $\rho \sim 0.1\rho_0$ [52]. On the other hand, HO argue in Ref. [24] that the MNA channels are required to describe the high-momentum tails of the proton momentum spectra from \bar{p} annihilation at $p_{\text{lab}} = 608$ MeV/c on ^{12}C [54]. However, the intranuclear cascade calculations [55] and the GiBUU calculations [22] have demonstrated that the agreement with the data [54] can be reached without any unusual mechanisms.

Using a diagram language, HO have considered $\bar{p}N$ annihilation vertices including virtual pions which may decay into particle-hole excitations [23–25]. These diagrams can be interpreted as MNA channels, which, according to the HO calculations, have extremely high probability at $\rho \sim \rho_0$, one order of magnitude higher than the ordinary SNA channels. This result is in a clear contradiction with the theoretical estimates by Cugnon and Vandermeulen [42, 43] and by Mishustin *et al.* [18], although these estimates are based on relatively simple statistical considerations. In our opinion, the HO calculations have a problem with convergence of the series in powers of ρ at $\rho \geq \rho_0$ (Eq. (4.3) in Ref. [24]). Because it is very difficult to test the MNA probability at $\rho \sim \rho_0$ experimentally, different theoretical predictions are still possible here.

In Ref. [18], the relative importance of MNA channels was evaluated by calculating the probability of finding more than one nucleon in the annihilation volume V_{ann} . This calculation was done for a spherical volume with the radius $R_{\text{ann}} \simeq 0.8$ fm assuming the Poisson distribution in the number of nucleons n , $P(n) = \bar{n}^n \exp(-\bar{n})/n!$, where $\bar{n} = \rho V_{\text{ann}}$ is the average number of nucleons in this volume. In the case of enhanced density, $\rho \simeq 2\rho_0$, one has $\bar{n} \simeq 0.6$. This leads to the probability of MNA channels with $n > 1$ on the level of 40% of the SNA ($n = 1$), which is about one order of magnitude smaller than the value predicted in Refs. [23–25].

In the literature, one can also find other arguments against a large enhancement of $\bar{p}N$ annihilation cross section in nuclear medium. For instance, as argued in Refs. [44,45], the presence of additional nucleon(s) in the annihilation volume may lead to the ‘‘screening’’ of in-medium annihilation as compared to the usual SNA mechanism. By introducing the screening effect these authors achieve a better agreement with experimental data on \bar{p} production in pA and AA collisions at AGS energies.

To illustrate the influence of the in-medium effective masses on the antiproton annihilation, let us consider a relatively simple case of the two-pion annihilation $\bar{p}p \rightarrow \pi^- \pi^+$. In vacuum, this process can be described by the one-nucleon exchange model [56,57]. In the Born approximation, the matrix element can be written as follows:

$$M = -2F^2(t)\bar{v}(m_{s_{\bar{p}}}, p_{\bar{p}})[A - \not{k}B(t)]u(m_{s_p}, p_p), \quad (12)$$

where u and v are, respectively, the proton and antiproton bispinors ($\bar{u}u = 1$, $\bar{v}v = -1$), which depend on the spin magnetic quantum numbers $m_{s_p}, m_{s_{\bar{p}}}$ and on the four momenta $p_p, p_{\bar{p}}$, and k is the four-momentum of π^+ . The scalar parameters A and B are defined as

$$A = \frac{f^2}{m_\pi^2} 2m_N, \quad B(t) = \frac{f^2}{m_\pi^2} \left(1 + \frac{4m_N^2}{t - m_N^2} \right), \quad (13)$$

where $f = 1.008$ is the pion-nucleon coupling constant and $t = (p_p - k)^2$. The factor of -2 in Eq. (12) is obtained from an isospin algebra. The off-shell nucleon form factor is chosen as in Ref. [56]:

$$F(t) = \left(\frac{\Lambda^2 - m_N^2}{\Lambda^2 - t} \right)^{1/2}, \quad (14)$$

where Λ is a cutoff parameter. In the center-of-mass (c.m.) frame, the differential cross section of the process $\bar{p}p \rightarrow \pi^- \pi^+$ is

$$\frac{d\sigma_{\bar{p}p \rightarrow \pi^- \pi^+}}{d\Omega_{\text{c.m.}}} = \frac{(2m_N)^2}{64\pi^2 s} \frac{|M|^2 q_{\pi\pi}}{q_{\bar{p}p}}, \quad (15)$$

where $s = (p_{\bar{p}} + p_p)^2$, $q_{\bar{p}p} = q(\sqrt{s}, m_N)$, and $q_{\pi\pi} = q(\sqrt{s}, m_\pi)$ are the c.m. momenta of the incoming and outgoing particles, respectively, with $q(\sqrt{s}, m) = (s/4 - m^2)^{1/2}$ and $|M|^2 = \frac{1}{4} \sum_{m_{s_{\bar{p}}}, m_{s_p}} |M|^2$.

The solid line in Fig. 13 reports the total vacuum $\bar{p}p \rightarrow \pi^- \pi^+$ cross section calculated in the Born approximation. This is a quite rough approximation in the case of $\bar{p}p$ incoming channel. We stress, however, that our main purpose here is just to demonstrate the influence of the in-medium effects and not to perform state-of-the-art calculations for the two-pion annihilation in vacuum. To fit the data for slow antiprotons ($p_{\text{lab}} < 1$ GeV/c), we have chosen a rather small value of the cutoff parameter $\Lambda = 1.0$ GeV because the initial-state interactions are neglected (see discussion in Refs. [56,57]).

Assuming for simplicity the G -parity transformed proton scalar and vector potentials acting on the antiproton, the baryonic mean fields can be now taken into account by replacing $m_N \rightarrow m_N^*$, $p_p \rightarrow p_p^*$, $p_{\bar{p}} \rightarrow p_{\bar{p}}^*$, $s \rightarrow s^* = (p_p^* + p_{\bar{p}}^*)^2$, and $t \rightarrow t^* = (p_p^* - k)^2$ in Eqs. (12), (13), and (15) (cf. Refs. [50,63]). Note that we always keep the vacuum

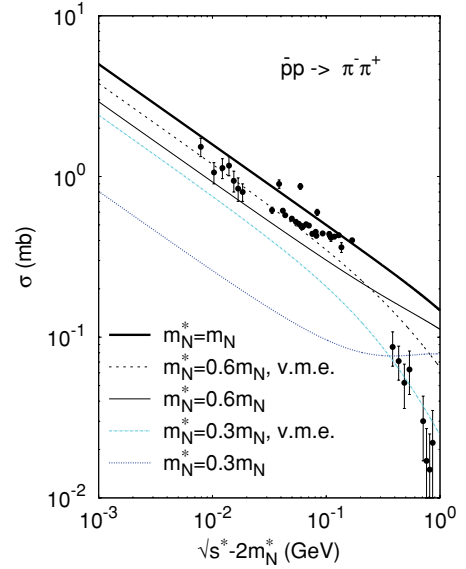


FIG. 13. (Color online) The cross section of the process $\bar{p}p \rightarrow \pi^- \pi^+$ as a function of the total in-medium c.m. kinetic energy $\sqrt{s^* - 2m_N^*}$. The results are shown for the different choices of a nucleon effective mass m_N^* . The calculation with $m_N^* = m_N$ (thick solid line) corresponds to the vacuum cross section, which has to be compared with experimental data. The calculations with $m_N^* = 0.6m_N$ (thin solid line, full result; dashed line, vacuum matrix element) and $m_N^* = 0.3m_N$ (dotted line, full result; dash-dotted line, vacuum matrix element) represent the in-medium cross sections. Experimental data are from Refs. [58–62].

nucleon mass in the numerator $\Lambda^2 - m_N^2$ of the form factor (14) because the preceding replacements are motivated by the baryon in-medium self-energies that should not change the form factor fixed in vacuum. Then the total in-medium $\bar{p}p \rightarrow \pi^- \pi^+$ cross section reads

$$\begin{aligned} \sigma_{\bar{p}p \rightarrow \pi^- \pi^+}^{\text{med}}(\sqrt{s^*}) &= \frac{(2m_N^*)^2 q(\sqrt{s^*}, m_\pi)}{32\pi s^* q(\sqrt{s^*}, m_N^*)} \\ &\times \int_{-1}^1 d \cos \Theta_{\text{c.m.}} \overline{|M^{\text{med}}|^2}(\sqrt{s^*}, \cos \Theta_{\text{c.m.}}). \end{aligned} \quad (16)$$

Here the quantity M^{med} is the in-medium matrix element, while $\Theta_{\text{c.m.}}$ is the angle between the proton and π^+ three momenta in the c.m. frame. The results of calculation using Eq. (16) at $m_N^* = 0.6m_N$ ($\rho = \rho_0$) and $m_N^* = 0.3m_N$ ($\rho \simeq 2\rho_0$) are shown in Fig. 13 by the thin solid and dotted lines, respectively. As one can see, the in-medium $\bar{p}p \rightarrow \pi^- \pi^+$ cross section is strongly reduced, largely due to the $(2m_N^*)^2$ factor in Eq. (16), which comes from the in-medium Dirac bispinor normalization. For orientation, we present in Fig. 14 the baryon density dependence of the nucleon effective mass m_N^* and of the nucleon scalar density ρ_S (see Eqs. (8), (9), and (15) in Ref. [26]). The effective mass m_N^* drops with increasing baryon density, which is an important effect influencing in-medium cross sections (see also Refs. [47–50]).

The two-pion annihilation channels represent, however, less than 1% of the total annihilation cross section, while the

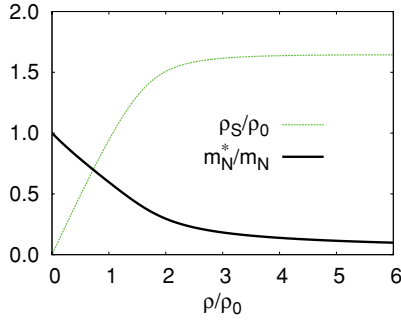


FIG. 14. (Color online) Nucleon effective mass and scalar density vs the baryon density in infinite nuclear matter in the case of NL3 interaction [30] applied in the present work.

direct calculation of multimeson annihilation matrix elements is impossible. We will assume that the matrix elements are not modified in nuclear medium and take into account only the in-medium bispinor normalization, flux, and phase space volume. This intuitive assumption has some support from the earlier studies of $NN \rightarrow NN$ and $NN \rightarrow N\Delta$ cross sections in nuclear matter [47–50]. In this way, one can write the following formula for the in-medium cross section of the $\bar{N}N \rightarrow M_1, M_2, \dots, M_n$ annihilation channel with n outgoing mesons (cf. Refs. [26,28,64]):

$$\sigma_{\bar{N}N \rightarrow M_1, M_2, \dots, M_n}^{\text{med}}(\sqrt{s^*}) = \sigma_{\bar{N}N \rightarrow M_1, M_2, \dots, M_n}(\sqrt{s_{\text{corr}}}) \left(\frac{m_N^*}{m_N} \right)^2 \times \frac{I_{\bar{N}N}}{I_{\bar{N}N}^*} \frac{\Phi_n(\sqrt{s^*}; m_1, m_2, \dots, m_n)}{\Phi_n(\sqrt{s_{\text{corr}}}; m_1, m_2, \dots, m_n)}. \quad (17)$$

Here m_1, m_2, \dots, m_n are the vacuum masses of outgoing mesons, $\sqrt{s_{\text{corr}}} = \sqrt{s^*} - 2(m_N^* - m_N)$ is the so-called corrected invariant energy of the colliding particles, the analog of the invariant energy in vacuum. The quantities $I_{\bar{N}N} = q(\sqrt{s_{\text{corr}}}, m_N)\sqrt{s_{\text{corr}}}$ and $I_{\bar{N}N}^* = q(\sqrt{s^*}, m_N^*)\sqrt{s^*}$ are the vacuum and in-medium flux factors, respectively. The n -body phase space volume is defined as

$$\Phi_n(\sqrt{s}; m_1, m_2, \dots, m_n) = \int \frac{d^3k_1}{(2\pi)^3 2\omega_1} \int \frac{d^3k_2}{(2\pi)^3 2\omega_2} \dots \int \frac{d^3k_n}{(2\pi)^3 2\omega_n} \times \delta^{(4)}(\mathcal{P} - k_1 - k_2 - \dots - k_n), \quad (18)$$

where $\mathcal{P}^2 = s$ and $\omega_i^2 - \mathbf{k}_i^2 = m_i^2$ ($i = 1, 2, \dots, n$). The quantity $\sigma_{\bar{N}N \rightarrow M_1, M_2, \dots, M_n}(\sqrt{s_{\text{corr}}})$ is the vacuum cross section. Application of Eq. (17) to the process $\bar{p}p \rightarrow \pi^- \pi^+$ leads to the formula (16) with replacement $|M^{\text{med}}|^2(\sqrt{s^*}, \cos \Theta_{\text{c.m.}}) \rightarrow |M|^2(\sqrt{s_{\text{corr}}}, \cos \Theta_{\text{c.m.}})$. The results obtained using Eq. (17) for $m_N^* = 0.6m_N$ and $m_N^* = 0.3m_N$ are shown in Fig. 13 by the dashed and dash-dotted lines, respectively. The conclusion is that using vacuum matrix element produces somewhat less-pronounced in-medium reduction of the cross section.

To simulate the mean-field effects on the total annihilation cross section, we represent it as a sum of partial annihilation cross sections with various outgoing mesonic channels. In practice, this is done by using the statistical annihilation

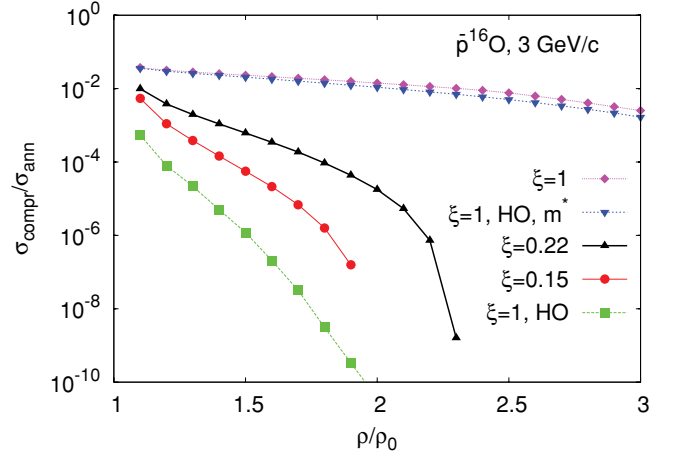


FIG. 15. (Color online) Probability of \bar{p} annihilation at $\rho_{\text{max}} > \rho$ vs ρ for $\bar{p}^{16}\text{O}$ collisions at $p_{\text{lab}} = 3 \text{ GeV}/c$. The calculations with various values of the reduction factor ξ and vacuum $\bar{p}N$ annihilation cross section are shown by lines with points denoted by the values of ξ only. The calculation with the in-medium enhanced $\bar{p}N$ annihilation probability by the HO formula [Eq. (5) in Ref. [25] with parameters taken at the \bar{p} kinetic energy of 50 MeV] and $\xi = 1$ are shown by the dashed line with solid boxes. The result taking into account both the HO formula and the mean-field reduction of the $\bar{p}N$ annihilation cross section according to Eq. (17) is shown by the dashed line with upside-down solid triangles. The calculations for $\rho \leq \rho_0$ are not shown because they are influenced by the finite size of the $(r, p, \cos \Theta)$ grid in the space of the antiproton radial position r , momentum p , and $\cos \Theta = \mathbf{rp}/rp$ (see Sec. II).

model of Refs. [65,66]. Then we apply Eq. (17) to every annihilation channel with up to $n = 6$ outgoing mesons. The mean-field effects on the annihilation channels with more than six outgoing mesons are neglected.

In the following GiBUU calculations of the present section, we keep the first stage (see Sec. II) unchanged: It is always computed with the reduction factor $\xi = 0.22$ and vacuum $\bar{p}N$ annihilation cross sections. This is reasonable because the compressional response of a nuclear system on a fast-moving antiproton is weak and can be neglected. The in-medium corrections to the $\bar{p}N$ annihilation cross section should also weaken for the fast antiproton. Thus, we vary the model parameters for the second-stage compressional dynamics only.

Figure 15 shows the probability of \bar{p} annihilation at $\rho_{\text{max}} > \rho$ as a function of ρ for the inclusive set of $\bar{p}^{16}\text{O}$ events at the beam momentum of 3 GeV/c. First, we study the influence of the reduction factor ξ of antiproton-meson coupling constants on the ACZ probability. To this aim, we have performed additional calculations by choosing $\xi = 0.15$ [$\text{Re}(V_{\text{opt}}) = -105 \text{ MeV}$] and $\xi = 1$ [$\text{Re}(V_{\text{opt}}) = -677 \text{ MeV}$], where the values of the Schrödinger equivalent potential at $E_{\text{lab}} = 0$ (see Ref. [22] for details) in the center of the ^{16}O nucleus are given in brackets. We recall that our default value $\xi = 0.22$ [$\text{Re}(V_{\text{opt}}) = -153 \text{ MeV}$] is motivated by the best agreement of the GiBUU calculations [22] with the measured antiproton absorption cross sections on nuclei. The value $\xi = 0.15$ is in line with the results of \bar{p} -atomic X-ray transitions and

radiochemical data analysis [19], while the extreme choice of $\xi = 1$ corresponds to the G -parity transformed nucleon mean fields. As expected, larger (smaller) values of ξ give rise to larger (smaller) ACZ probability at a given ρ . Results are quite sensitive to the antiproton-meson coupling constants. For instance, at $\rho = 2\rho_0$, the ACZ probability is equal to zero in the case of $\xi = 0.15$; that is, the maximum nucleon density does not reach the value of $2\rho_0$ at all with this value of ξ . At the same time, for $\xi = 1$, the ACZ probability is $\sim 10^{-2}$ at $\rho = 2\rho_0$, which is three orders of magnitude larger than for $\xi = 0.22$.

Finally, we discuss the sensitivity of our results to the choice of the in-medium annihilation cross section related to the imaginary part of the antiproton optical potential

$$\text{Im}(V_{\text{opt}}) = -\frac{1}{2}\langle v_{\text{rel}}\sigma_{\text{tot}}^{\text{med}}\rangle\rho. \quad (19)$$

Here, $\sigma_{\text{tot}}^{\text{med}}$ is the total in-medium $\bar{p}N$ cross section, which includes both (in-medium) annihilative and Pauli-blocked nonannihilative contributions. Note that in distinction to Eq. (7) for the annihilation width, Eq. (19) contains the *total* $\bar{p}N$ cross section. Applying Eq. (19) for the case of the HO formula for the annihilation probability per unit length (see Eq. (5) in Ref. [25]) leads to an extremely deep imaginary part of the antiproton optical potential, $\text{Im}(V_{\text{opt}}) \simeq -(1200-1700)$ MeV at the center of the ^{16}O nucleus, with the uncertainty due to the antiproton mean field. This is more than one order of magnitude larger than the value $\text{Im}(V_{\text{opt}}) \simeq -107$ MeV in our default choice of model parameters [22].

At this point, certainly, one wishes to get some phenomenological estimates of the antiproton-nucleus potential depths. Unfortunately, it is very hard to get stringent phenomenological constraints on the optical potential of a hadron at the nuclear center [67]. As has been known for a long time from pionic atoms and low-energy pion nucleus scattering, the different density shapes of the potential give the same result for the atomic and scattering data, while they strongly differ at $\rho = \rho_0$ [68,69]. In a similar way, the \bar{p} -nucleus scattering and absorption cross sections (see [70–72] and references therein) and the \bar{p} -atomic data analysis [19,67,73] result in quite uncertain real and imaginary parts of the \bar{p} optical potential at the nuclear center $\text{Im}(V_{\text{opt}}) = -(70-150)$ MeV and $\text{Re}(V_{\text{opt}}) = -(0-100)$ MeV. We stress that the actual uncertainty in the potential depths may be much bigger due to the extrapolation from the far periphery of a nucleus using some assumed relation between the nuclear density and potential. Nevertheless, the known phenomenological values are in a fair agreement with our default model inputs.

As one can see from Fig. 15, using the HO formula leads to eight orders of magnitude smaller ACZ probability at $\rho = 2\rho_0$ as compared to the calculation with the vacuum annihilation cross section (see the lines with solid boxes and with solid diamonds). This is not surprising because the ρ -dependent terms in Eq. (5) of Ref. [25] strongly enhance the annihilation rate at high densities. However, as discussed earlier, the mean-field and phase-space effects should reduce the annihilation rate.

Now we implement both effects simultaneously by introducing corresponding multiplicative factors to the vacuum

$\bar{p}N$ annihilation cross section. The resulting ACZ probability increases by eight orders of magnitude with respect to the one given by the HO effect alone (see the lines with upside-down solid triangles and with solid boxes in Fig. 15), that is, practically brings it back to the original calculation with the vacuum annihilation cross section. Certainly, this is only a rough estimate of the in-medium effects in the annihilation cross section. In our opinion, the full calculation in the spirit of Refs. [23–25], but taking into account also the baryonic mean fields, is needed to obtain the realistic values for the antiproton width at high nucleon densities.

In spite of large uncertainties in the in-medium properties of antiproton, we think that our standard choice of the model parameters, that is, the vacuum $\bar{p}N$ annihilation cross section and the reduction factor $\xi = 0.22$, is quite reasonable for the present study of compressional effects. As has been shown within the GiBUU model in Ref. [22], this set of parameters accounts for the \bar{p} absorption data on nuclei at $p_{\text{lab}} < 1$ GeV/ c and pion and proton production data from \bar{p} annihilation on nuclei at 608 MeV/ c .

VI. SUMMARY AND OUTLOOK

We have generalized our previous analysis of the nuclear compression dynamics induced by an antiproton at rest [26] to the case of a moving antiproton. The \bar{p} -nucleus collisions at the beam momenta of 0.3–10 GeV/ c have been simulated within the transport GiBUU model [27] with relativistic mean fields. In our two-stage calculational scheme, we apply, first, the standard parallel ensemble mode of GiBUU to determine the antibaryon coordinates and momenta at the annihilation point. We have studied in detail the coordinate and momentum distributions of annihilation points at different beam momenta. This calculation is performed to evaluate the probability that the antibaryon has been slowed down and reached the nuclear interior before annihilation. Those rare events that satisfy these conditions are used as the input for a more detailed calculation. Namely, we perform the coherent GiBUU runs [26] initializing the antiproton at the given momentum and position inside the nucleus and following the evolution of the \bar{p} -nucleus system. In the coherent mode, the antibaryon-nucleon annihilation channels are switched off, but, instead, the survival probability of the antiproton is determined as a function of time. This makes it possible to trace the compression process of the \bar{p} -nucleus system in time and determine the probability of \bar{p} annihilation in the compressed nuclear configuration with the maximum nuclear density $\rho_{\text{max}} \geq 2\rho_0$.

The results of our study are quite sensitive to the actual strengths of the real and imaginary parts of the antiproton optical potential. For example, by choosing $\text{Re}[V_{\text{opt}}(\rho_0)] - 100$ MeV instead of our default $\text{Re}[V_{\text{opt}}(\rho_0)] - 150$ MeV reduces the ACZ probability by two orders of magnitude. The -100 MeV value of the real part of the antiproton optical potential is consistent with the X-ray data from antiprotonic atoms and radiochemical data [19], while the -150 MeV value is favored by GiBUU calculations of the antiproton absorption cross sections on nuclei and of the pion and proton momentum spectra from \bar{p} annihilation on nuclei [22]. Another important source of uncertainty is given by the

value of $\text{Im}[V_{\text{opt}}(\rho_0)]$. In our standard calculations, we adopt $\text{Im}[V_{\text{opt}}(\rho_0)] \simeq -100$ MeV, which follows from a simple $t\rho$ approximation and is consistent with $\text{Re}[V_{\text{opt}}(\rho_0)] \simeq -150$ MeV, as shown in Ref. [22]. However, according to the model of Hernández and Oset [23–25], the antiproton annihilation rate is increased by about one order of magnitude with respect to the simple $t\rho$ approximation, even at the normal nuclear matter density. This will result in $\text{Im}[V_{\text{opt}}(\rho_0)] \simeq -1500$ MeV, which is well beyond the phenomenological expectations. If this were, indeed, the case, the ACZ probability would be five to eight orders of magnitude smaller than in our standard calculations.

With all these reservations in mind, we now summarize the results of our standard calculations which use the phenomenological input parameters for the antiproton-nucleus interaction. In general, antiproton initializations in a central nuclear region with momenta of less or about the nucleon Fermi momentum lead to the maximum probability of annihilation in the compressed zone of the order of 10^{-3} – 10^{-1} . The uncertainty is caused by unknown spatial spread of the antiproton distribution function. When combined with the actual antibaryon positions and momenta at the annihilation points determined from the first-stage GiBUU simulation, this results in the ACZ probability $\sim 10^{-5}$ – 10^{-3} for the beam momenta of 3–10 GeV/ c . We have found that, within this beam momentum range, the excitation function of the ACZ probability is very flat (cf. Figs. 7 and 8). Therefore, the range $p_{\text{lab}} = 3$ –10 GeV/ c is quite well suited for the study of compressed nuclear systems. The beam momenta of about 1 GeV/ c are clearly disfavored because the antiproton is not decelerated enough due to the smallness of the $\bar{N}N$ inelastic production cross section. At $p_{\text{lab}} < 1$ GeV/ c , the ACZ probability increases with decreasing beam momentum. However, additional triggers demanding a fast proton [21] or large energy deposition [40,41] are not very efficient for ACZ selection at small beam momenta. At the same time, we have found that these triggers increase the ACZ probability by more than one order of magnitude in the beam momentum range of 3–10 GeV/ c . Such antiproton beams will be available at

FAIR, which would be the ideal place to search for the nuclear compression effects induced by antibaryons. By taking the expected luminosity $L = 2 \times 10^{32}$ cm $^{-2}$ s $^{-1}$ for the PANDA experiment at FAIR [21], the ACZ rate can be estimated as $Y = \sigma_{\text{compr}} L \sim 10^2$ – 10^3 s $^{-1}$, where $\sigma_{\text{compr}} \sim 10^{-3}$ – 10^{-2} mb is the ACZ cross section above 1 GeV/ c (see Fig. 7). Here we stress once again that, due to the presently not-well-known antiproton optical potential at $\rho \geq \rho_0$ and due to uncertain spatial spread of the antiproton distribution function, the preceding estimate of the ACZ rate has a rather large uncertainty.

We have also shown that the selection of small impact parameter events increases the ACZ probability by a factor of 2–3. This selection could be reached, for example, by triggering on the events with a small azimuthal asymmetry of secondary particles.

Some signals associated with the ACZ events have already been discussed in Refs. [18,26]. Unfortunately, however, no unique signal suggested so far can alone be sufficient to identify the nuclear compression unambiguously. Therefore, we believe that the combination of different signals, for example, emission of a fast proton plus large collective flow energy of the nuclear fragments, would be a more promising strategy to search for the ACZ events. Certainly, further theoretical studies are needed to find the experimentally realizable ways of observing nuclear compression in \bar{p} -nucleus collisions, in particular at FAIR energies.

ACKNOWLEDGMENTS

We gratefully acknowledge the support of the Frankfurt Center for Scientific Computing. We thank O. Buss, A. Gillitzer, B. O. Kerbikov, U. Mosel, J. Ritman, and I. A. Pshenichnov for stimulating discussions. This work was partially supported by the Helmholtz International Center for FAIR within the framework of the LOEWE program (Landes-offensive zur Entwicklung Wissenschaftlich-Ökonomischer Exzellenz) launched by the State of Hesse, by DFG Grant No. 436 RUS 113/957/0-1 (Germany), as well as Grants No. NS-7235.2010.2 and No. RFBR-09-02-91331 (Russia).

-
- [1] J. C. Collins and M. J. Perry, *Phys. Rev. Lett.* **34**, 1353 (1975).
 - [2] E. V. Shuryak, *Phys. Rep.* **61**, 71 (1980).
 - [3] P. Braun-Munzinger and J. Wambach, *Rev. Mod. Phys.* **81**, 1031 (2009).
 - [4] J. Hofmann, H. Stöcker, U. Heinz, W. Scheid, and W. Greiner, *Phys. Rev. Lett.* **36**, 88 (1976).
 - [5] K. Tanida *et al.*, *Phys. Rev. Lett.* **86**, 1982 (2001).
 - [6] J. Schaffner, C. B. Dover, A. Gal, C. Greiner, and H. Stöcker, *Phys. Rev. Lett.* **71**, 1328 (1993).
 - [7] J. Schaffner, C. B. Dover, A. Gal, C. Greiner, D. J. Millener, and H. Stöcker, *Ann. Phys.* **235**, 35 (1994).
 - [8] Y. Akaishi and T. Yamazaki, *Phys. Rev. C* **65**, 044005 (2002).
 - [9] R. S. Hayano *et al.* (KEK-E570 Collaboration), *Mod. Phys. Lett. A* **23**, 2505 (2008).
 - [10] J. Mares, E. Friedman, and A. Gal, *Nucl. Phys. A* **770**, 84 (2006).
 - [11] A. Ramos and E. Oset, *Nucl. Phys. A* **671**, 481 (2000).
 - [12] E. Oset and H. Toki, *Phys. Rev. C* **74**, 015207 (2006).
 - [13] T. Hyodo and W. Weise, *Phys. Rev. C* **77**, 035204 (2008).
 - [14] A. Dote, T. Hyodo, and W. Weise, *Phys. Rev. C* **79**, 014003 (2009).
 - [15] Y. Akaishi, T. Yamazaki, M. Obu, and M. Wada, *Nucl. Phys. A* **835**, 67 (2010).
 - [16] T. Yamazaki *et al.*, *Phys. Rev. Lett.* **104**, 132502 (2010).
 - [17] T. J. Bürvenich, I. N. Mishustin, L. M. Satarov, J. A. Maruhn, H. Stöcker, and W. Greiner, *Phys. Lett. B* **542**, 261 (2002).
 - [18] I. N. Mishustin, L. M. Satarov, T. J. Bürvenich, H. Stöcker, and W. Greiner, *Phys. Rev. C* **71**, 035201 (2005).
 - [19] E. Friedman, A. Gal, and J. Mareš, *Nucl. Phys. A* **761**, 283 (2005).
 - [20] J. Pochodzalla, *Phys. Lett. B* **669**, 306 (2008).
 - [21] The PANDA Collaboration, M. F. M. Lutz, B. Pire, O. Scholten, and R. Timmermans, *arXiv:0903.3905*.
 - [22] A. B. Larionov, I. A. Pshenichnov, I. N. Mishustin, and W. Greiner, *Phys. Rev. C* **80**, 021601 (2009).

- [23] E. Hernández and E. Oset, *Phys. Lett. B* **181**, 207 (1986).
- [24] E. Hernández and E. Oset, *Nucl. Phys. A* **493**, 453 (1989).
- [25] E. Hernández and E. Oset, *Z. Phys. A* **341**, 201 (1992).
- [26] A. B. Larionov, I. N. Mishustin, L. M. Satarov, and W. Greiner, *Phys. Rev. C* **78**, 014604 (2008).
- [27] [<http://gibuu.physik.uni-giessen.de/GiBUU>].
- [28] A. B. Larionov, O. Buss, K. Gallmeister, and U. Mosel, *Phys. Rev. C* **76**, 044909 (2007).
- [29] T. Gaitanos, H. Lenske, and U. Mosel, *Phys. Lett. B* **663**, 197 (2008).
- [30] G. A. Lalazissis, J. König, and P. Ring, *Phys. Rev. C* **55**, 540 (1997).
- [31] J. Aichelin, *Phys. Rep.* **202**, 233 (1991).
- [32] A. Dote, Y. Akaishi, and T. Yamazaki, *Nucl. Phys. A* **754**, 391 (2005).
- [33] I. N. Mishustin and A. B. Larionov, *Hyperfine Interact.* **194**, 263 (2009).
- [34] L. Montanet *et al.* (Particle Data Group), *Phys. Rev. D* **50**, 1173 (1994).
- [35] J. Rafelski, *Phys. Lett. B* **91**, 281 (1980).
- [36] P. Salvini, A. Panzarasa, and G. Bendiscioli, *Nucl. Phys. A* **760**, 349 (2005).
- [37] G. Bendiscioli, T. Bressani, L. Lavezzi, A. Panzarasa, and P. Salvini, *Nucl. Phys. A* **815**, 67 (2009).
- [38] H. Stöcker and W. Greiner, *Phys. Rep.* **137**, 277 (1986).
- [39] J. Cugnon and J. Vandermeulen, *Ann. Phys. (France)* **14**, 49 (1989).
- [40] M. R. Clover, R. M. DeVries, N. J. DiGiacomo, and Y. Yariv, *Phys. Rev. C* **26**, 2138 (1982).
- [41] J. Cugnon and J. Vandermeulen, *Nucl. Phys. A* **445**, 717 (1985).
- [42] J. Cugnon and J. Vandermeulen, *Phys. Lett. B* **146**, 16 (1984).
- [43] J. Cugnon and J. Vandermeulen, *Phys. Rev. C* **39**, 181 (1989).
- [44] S. H. Kahana, Y. Pang, T. Schlagel, and C. B. Dover, *Phys. Rev. C* **47**, 1356 (1993).
- [45] Y. Pang, D. E. Kahana, and S. H. Kahana, *Phys. Rev. Lett.* **78**, 3418 (1997).
- [46] C. Spieles, M. Bleicher, A. Jahns, R. Mattiello, H. Sorge, H. Stöcker, and W. Greiner, *Phys. Rev. C* **53**, 2011 (1996).
- [47] V. R. Pandharipande and S. C. Pieper, *Phys. Rev. C* **45**, 791 (1992).
- [48] C. Fuchs, A. Faessler, and M. El-Shabshiry, *Phys. Rev. C* **64**, 024003 (2001).
- [49] B. ter Haar and R. Malfliet, *Phys. Rev. C* **36**, 1611 (1987).
- [50] A. B. Larionov and U. Mosel, *Nucl. Phys. A* **728**, 135 (2003).
- [51] B. M. Pontecorvo, *Zh. Eksp. Teor. Fiz.* **30**, 947 (1956).
- [52] E. D. Minor, T. A. Armstrong, B. Chen, R. A. Lewis, and G. A. Smith, *Z. Phys. A* **342**, 447 (1992).
- [53] P. Montagna *et al.* (Obelix Collaboration), *Nucl. Phys. A* **700**, 159 (2002).
- [54] P. L. McGaughey *et al.*, *Phys. Rev. Lett.* **56**, 2156 (1986).
- [55] J. Cugnon, P. Deneye, and J. Vandermeulen, *Nucl. Phys. A* **500**, 701 (1989).
- [56] B. Moussallam, *Nucl. Phys. A* **407**, 413 (1983).
- [57] B. Moussallam, *Nucl. Phys. A* **429**, 429 (1984).
- [58] P. S. Eastman *et al.*, *Nucl. Phys. B* **51**, 29 (1973).
- [59] T. Tanimori *et al.*, *Phys. Rev. Lett.* **55**, 1835 (1985).
- [60] G. Bardin *et al.*, *Phys. Lett. B* **192**, 471 (1987).
- [61] Y. Sugimoto *et al.*, *Phys. Rev. D* **37**, 583 (1988).
- [62] G. Bardin *et al.*, *Nucl. Phys. B* **411**, 3 (1994).
- [63] H. Kim, S. Schramm, and S. H. Lee, *Phys. Rev. C* **56**, 1582 (1997).
- [64] M. Wagner, A. B. Larionov, and U. Mosel, *Phys. Rev. C* **71**, 034910 (2005).
- [65] E. S. Golubeva, A. S. Iljinov, B. V. Krippa, and I. A. Pshenichnov, *Nucl. Phys. A* **537**, 393 (1992).
- [66] I. A. Pshenichnov, doctoral thesis, INR, Moscow, 1998.
- [67] E. Friedman and A. Gal, *Phys. Rep.* **452**, 89 (2007).
- [68] R. Seki and K. Masutani, *Phys. Rev. C* **27**, 2799 (1983).
- [69] E. Friedman, *Phys. Rev. C* **28**, 1264 (1983).
- [70] O. D. Dalkarov and V. A. Karmanov, *Nucl. Phys. A* **445**, 579 (1985).
- [71] S. Janouin *et al.*, *Nucl. Phys. A* **451**, 541 (1986).
- [72] E. Friedman and J. Lichtenstadt, *Nucl. Phys. A* **455**, 573 (1986).
- [73] C. Y. Wong, A. K. Kerman, G. R. Satchler, and A. D. Mackellar, *Phys. Rev. C* **29**, 574 (1984).